Localized Electric Field of Plasmonic Nanoplatform Enhanced Photodynamic Tumor Therapy

Yiye Li,[†,⊥] Tao Wen,[‡,⊥] Ruifang Zhao,[†] Xixi Liu,[†,§] Tianjiao Ji,[†] Hai Wang,[†] Xiaowei Shi,[‡] Jian Shi,[†] Jingyan Wei,[§] Yuliang Zhao,[†] Xiaochun Wu,*[,‡] and Guangjun Nie*[,†]

[†]CAS Key Laboratory for Biomedical Effects of Nanomaterials & Nanosafety, National Center for Nanoscience and Technology, Beijing 100190, China, [‡]CAS Key Laboratory of Standardization and Measurement for Nanotechnology, National Center for Nanoscience and Technology, Beijing 100190, China, and [§]College of Pharmaceutical Science, Jilin University, Changchun 130021, China. [⊥]Y.L. and T.W. contributed equally to this work.

ABSTRACT Near-infrared plasmonic nanoparticles demonstrate great potential in disease theranostic applications. Herein a nanoplatform, composed of mesoporous silica-coated gold nanorods (AuNRs), is tailor-designed to optimize the photodynamic therapy (PDT) for tumor based on the plasmonic effect. The surface plasmon resonance of AuNRs was fine-tuned to overlap with the exciton absorption of indocyanine green (ICG), a near-infrared photodynamic dye with poor photostability and low quantum yield. Such overlap greatly increases the singlet oxygen yield of incorporated ICG by maximizing the local field enhancement, and protecting the ICG molecules against photodegradation by virtue of the high absorption cross section of the AuNRs. The silica shell strongly increased ICG payload with the additional benefit of enhancing ICG photostability by facilitating the formation of ICG aggregates. As-fabricated AuNR@SiO$_2$—ICG nanoplatform enables trimodal imaging, near-infrared fluorescence from ICG, and two-photon luminescence/

photoacoustic tomography from the AuNRs. The integrated strategy significantly improved photodynamic destruction of breast tumor cells and inhibited the growth of orthotopic breast tumors in mice, with mild laser irradiation, through a synergistic effect of PDT and photothermal therapy. Our study highlights the effect of local field enhancement in PDT and demonstrates the importance of systematic design of nanoplatform to greatly enhancing the antitumor efficacy.
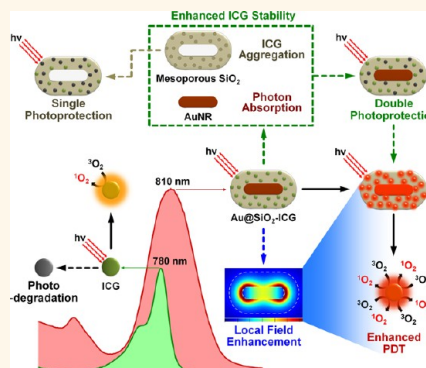
KEYWORDS: gold nanorod · local field enhancement · photosensitizer · photodynamic therapy · photothermal therapy

Because of their minimally invasive modalities, highly spatial and temporal controllability and specific lesion destruction, various photoactivatable theranostics hold great promise for addressing unmet medical needs.[1−3] Photodynamic therapy (PDT) is a photobased therapeutic modality with three essential components (light, photosensitizer and oxygen) for malignant cell killing by producing highly reactive oxygen species, especially singlet oxygen ($^1O_2$), when exposed to light of specific wavelength.[4,5] The efficacy of PDT depends almost entirely on the generation of $^1O_2$ created by photosensitizers after light absorption and subsequent transfer of the excited state energy to oxygen molecules.

In recent years, the electromagnetic near-field enhancement mechanism of plasmonic metals has been explored to control $^1O_2$ generation.[6−8] When the localized surface plasmon resonance (SPR) band is in resonance with the absorption band of vicinal photosensitizer, the absorption coefficient of the photosensitizer is greatly enhanced by localized electric field (LEF), and therefore, the production of $^1O_2$ is remarkably enhanced.[9] As a representative plasmonic metal nanomaterial with strong and tunable SPR and high biocompatibility, gold nanomaterial have been extensively explored for biomedical applications.[10−13] Most of the gold-based nanoplatforms use the plasmon-enhanced two photon luminescence and localized photothermal effect to improve bioimaging in parallel with localized hyperthermia for photothermal therapy (PTT) and photoenhanced chemotherapy, and mainly act as carriers for different photosensitizers in PDT.[14−22] However, utilizations
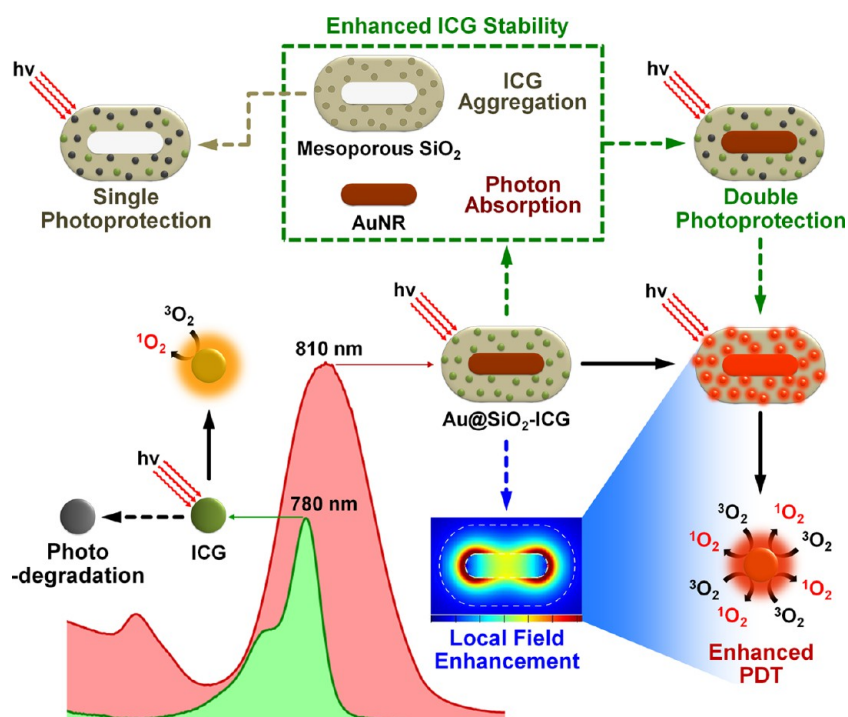
Scheme 1. Design of enhanced PDT by utilizing the surface plasmonic effect of the AuNR to simultaneously increase the absorption coefficient and reduce photodegradation of the photodynamic dye ICG. Mesoporous silica provided the second photoprotection for ICG by facilitating the formation of ICG aggregates. The double photoprotection will significantly enhance the stability of loaded-ICG in comparison with the single photoprotection of silica shell.

of their LEF enhancement to increase the production of $^1O_2$ in PDT are still scarce, especially lack of systematic study both *in vitro* and *in vivo*. Recently, a few attempts have preliminary demonstrated LEF effect of gold nanomaterial may be effective for improving PDT efficacy.[23,24]

Indocyanine green (ICG) is a near-infrared (NIR) tricarbocyanine dye approved by the US Food and Drug Administration (FDA) as a clinical imaging and diagnostic agent for assessing cardiac output, hepatic function, and ophthalmic angiography.[25–27] ICG has the intrinsic drawbacks of cyanine dyes, such as low quantum yield, poor photostability and thermal stability in aqueous solution, and rapid blood clearance.[27] Nevertheless, because of the remarkable NIR optical features within the optimized light-transparent window of biomedical applications, ICG has been intensively studied for NIR fluorescence imaging, and has also shown great potential in PDT and PTT when incorporated into various nanoplatforms,[18,28–35] where the improvement of the ICG stability and the resulting PDT is usually achieved by carrier encapsulation.

In this study, we design a nanoplatform, which composed of mesoporous silica-coated gold nanorods (AuNRs) incorporating ICG (Au@SiO$_2$–ICG), to optimize PDT efficacy based on the SPR effect of AuNR (Scheme 1). The longitudinal SPR band of AuNR was tuned to overlap with absorbance band of ICG. Because of enhanced LEF of the AuNR upon laser irradiation, the increased absorbance coefficient of the incorporated ICG can strongly enhance $^1O_2$ yield

without changing ICG payload. Furthermore, due to ∼10^6-fold higher absorption cross section of the AuNR compared to ICG, the AuNR acted as an effective light protecting agent to prevent ICG from photodegradation, as most of the irradiation photons at the overlap position are absorbed by the AuNR. Adsorption of ICG onto SiO$_2$ was found to lead to ICG aggregates and the aggregates exhibits much higher photostability and thermal stability than ICG monomers.[26,36,37] Therefore, the AuNR was coated with mesoporous SiO$_2$ to provide the second means of enhancing ICG stability by facilitating the formation of ICG aggregates. Meanwhile, the silica shell has additional benefits of increasing ICG payload by enlarging the nanoplatform surface area, providing a suitable spatial location to enable incorporated ICG to "feel" the local field enhancement, and protecting AuNRs from any aggregation-induced uncontrolled SPR peak shift. This nanoplatform was tailor-designed to greatly improve the low quantum yield and poor photostability stability of ICG. The resulting photodynamic effect of loaded-ICG is significantly enhanced with our integrated strategy. Furthermore, the nanoplatform possesses synergetic PTT effect based on both AuNR and ICG. The remarkable antitumor efficacy of this nanoplatform was demonstrated both *in vitro* and *in vivo*. Our study highlights the local field enhanced tumor PDT, and suggests that comprehensive integration of material characteristics with fine-tuned nanosystem opens new windows for designing powerful antitumor strategy.
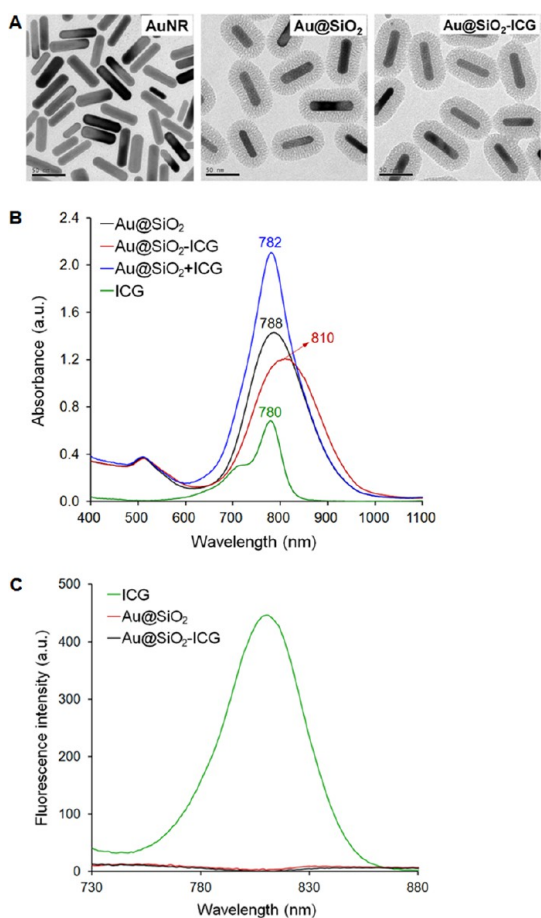
Figure 1. Characterization of Au@SiO₂—ICG. (A) TEM images of AuNR, Au@SiO₂ and Au@SiO₂—ICG. Scale bars, 50 nm. (B) UV—vis absorbance spectra of free ICG, Au@SiO₂, Au@SiO₂—ICG, and superposition of Au@SiO₂ and free ICG. (C) Fluorescence quenching of ICG in Au@SiO₂ confirmed by fluorescence spectra of free ICG, Au@SiO₂ and Au@SiO₂—ICG (Ex: 650 nm).

RESULTS AND DISCUSSION

Characterization of Au@SiO₂—ICG. Au@SiO₂ were synthesized according to Gorelikov and Matsuura's protocol with some modifications.[38] Transmission electron microscope (TEM) image showed that the AuNR core have a mean length of 49.0 ± 9.4 nm and width of 14.4 ± 2.0 nm. This corresponds to a mean aspect ratio of 3.4, giving a longitudinal SPR maximum around 780 nm and providing strong resonance coupling with ICG, the dye employed herein. The thickness of the silica shell in the longitudinal and transversal directions is 16.4 and 17.6 nm, respectively (Figure 1A). Using a single-step ultrasonic method, the loading content of ICG was estimated to be 7.9 wt %. As the surface of the Au@SiO₂ shell is negatively charged ($\delta = -28.2$ mV), adsorption of anionic ICG (Figure S1, Supporting Information) does not result from electrostatic interactions. ICG may interact with SiO₂ *via* hydrogen bonding between the O of the sulfonic group of ICG and the OH group on the silica surface. ICG in aqueous solution has one main peak at 780 nm and a shoulder at 710 nm

(Figure 1B). They correspond to the ICG monomer and H aggregate. The monomer peak matches well with the localized surface plasmon resonance (LSPR) peak of Au@SiO₂ at 788 nm (Figure 1B). After loading ICG, the LSPR peak of Au@SiO₂ slightly decreased with a red-shift to 810 nm. If the adsorbed states of the ICG exhibited no difference from its behavior in aqueous solution, the overall absorption spectrum of Au@-SiO₂—ICG should be the simple sum of pure ICG and Au@SiO₂, as shown by blue curve of Figure 1B, but this was not the case. The difference suggests that ICG formed aggregates upon adsorption onto the SiO₂ surface, in agreement with previous reports.[37] These UV/vis extinction spectra show the successful loading of ICG onto Au@SiO₂. The overlap of Au@SiO₂ and ICG peaks ensures local field enhanced PDT based on AuNR@SiO₂—ICG and potentially synergistic effect of PTT and PDT under irradiation with a single wavelength NIR laser. The formation of ICG aggregates was verified by negligible fluorescence from Au@SiO₂—ICG (Figure 1C). In aqueous solution, ICG tends to form more stable aggregates at high concentrations, and this is associated with a decline in monomer fluorescence.[39] If ICG did not form aggregates upon adsorption on SiO₂, enhanced ICG fluorescence would be observed due to MEF.[35,40] After adsorption saturation, free ICG will show luminescence (Figure S2). It further verifies that ICG adsorption induces the aggregation. To validate interaction between Au@SiO₂ and loaded fluorescent dyes, Rhodamine 6G (Rh6G) (Figure S3A), a photostable laser dye which is known to form aggregates after loading on SiO₂ nanoparticle,[41] was loaded onto Au@SiO₂ (Figure S3B). Fluorescence quenching similar to that of ICG was observed (Figure S3C). As we expected, the confirmed aggregation can greatly increase the photostability and thermal stability of incorporated ICG,[26,36] and further improve ICG-based PDT.

Cellular Uptake of Au@SiO₂—ICG. The optical properties of Au@SiO₂—ICG enable multimodal bioimaging. To study the cellular uptake of the nanoplatform, human breast carcinoma cell MDA-MB-231 were incubated with Au@SiO₂—ICG, Au@SiO₂ or free ICG for 24 h. Plasmon-enhanced two-photon luminescence of the AuNR core was used to assess the cellular uptake of Au@SiO₂—ICG. Two-photon-laser scanning confocal microscopy showed obvious luminescence in the cytoplasm after treatment with both Au@SiO₂—ICG and Au@SiO₂, suggesting the efficient cellular uptake and intracellular distribution of both nanomaterials (Figure 2A). It is notable that the fluorescence intensity in Au@SiO₂—ICG-treated cells is lower than that in Au@SiO₂-treated cells, exposed to the same concentration of Au@SiO₂. To investigate this further, quantitative measurements were carried out by comparing the elemental gold content of the cells treated with different formulations using inductively coupled plasma-mass spectrometry (ICP-MS). The elemental
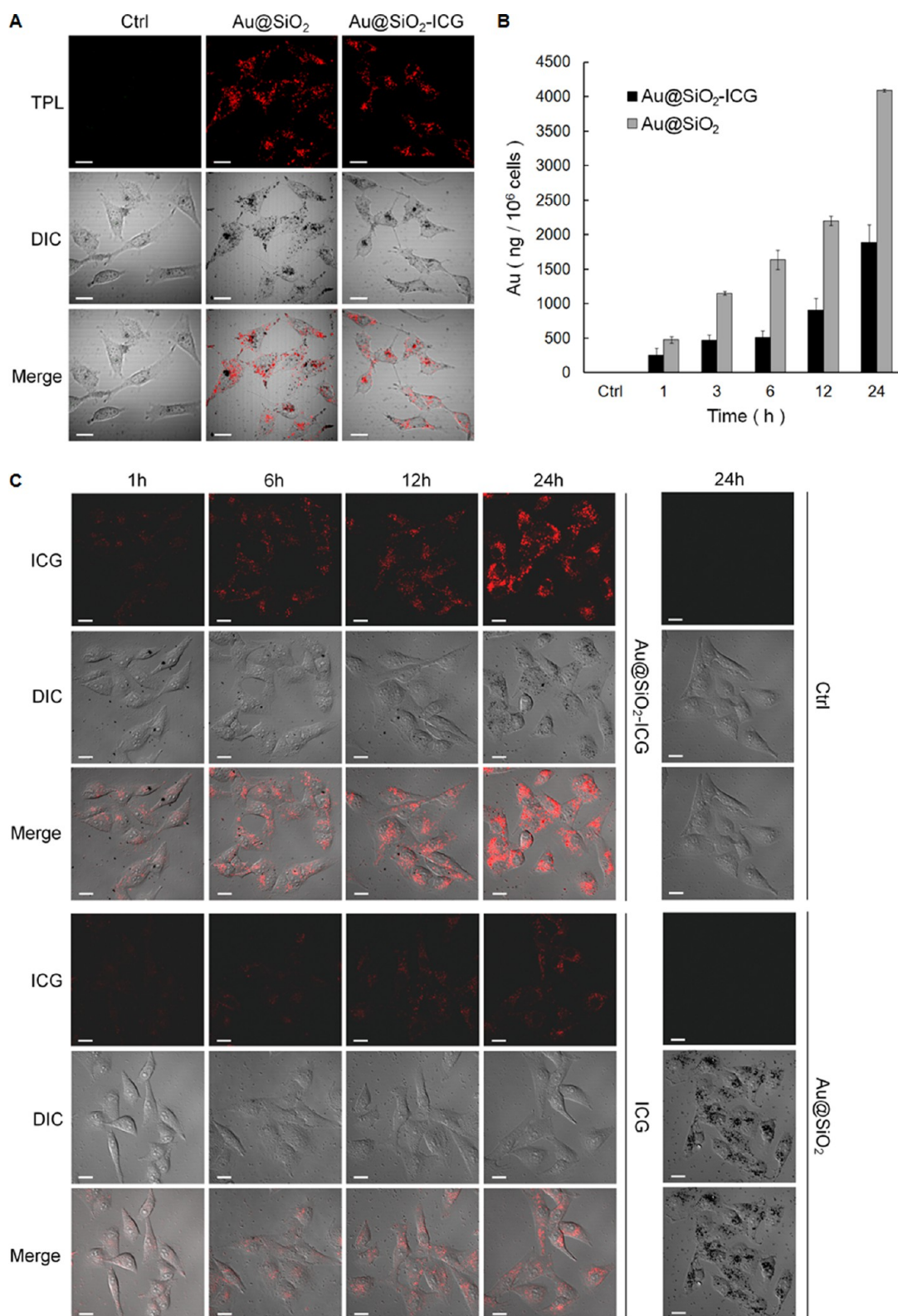
Figure 2. Cellular uptake of Au@SiO$_2$−ICG. (A) Two-photon-laser scanning confocal microscopy images of Au@SiO$_2$ and Au@SiO$_2$−ICG in MDA-MB-231 cells. Scale bars, 20 μm. (B) Quantification of Au levels by ICP-MS in MDA-MB-231 cells treated with Au@SiO$_2$ or Au@SiO$_2$−ICG. (C) Fluorescence images of ICG in MDA-MB-231 cells treated with Au@SiO$_2$−ICG and free ICG (Ex: 633 nm). Scale bars, 20 μm. The untreated cells were used as controls.

Au concentration of Au@SiO$_2$-treated cells was twice that of Au@SiO$_2$−ICG-treated cells at almost every incubation time point (Figure 2B). As the surface charge will

dramatically affect the cellular internalization of nanomaterials,[42] the zeta-potential of Au@SiO$_2$ was measured before and after ICG loading. Compared with
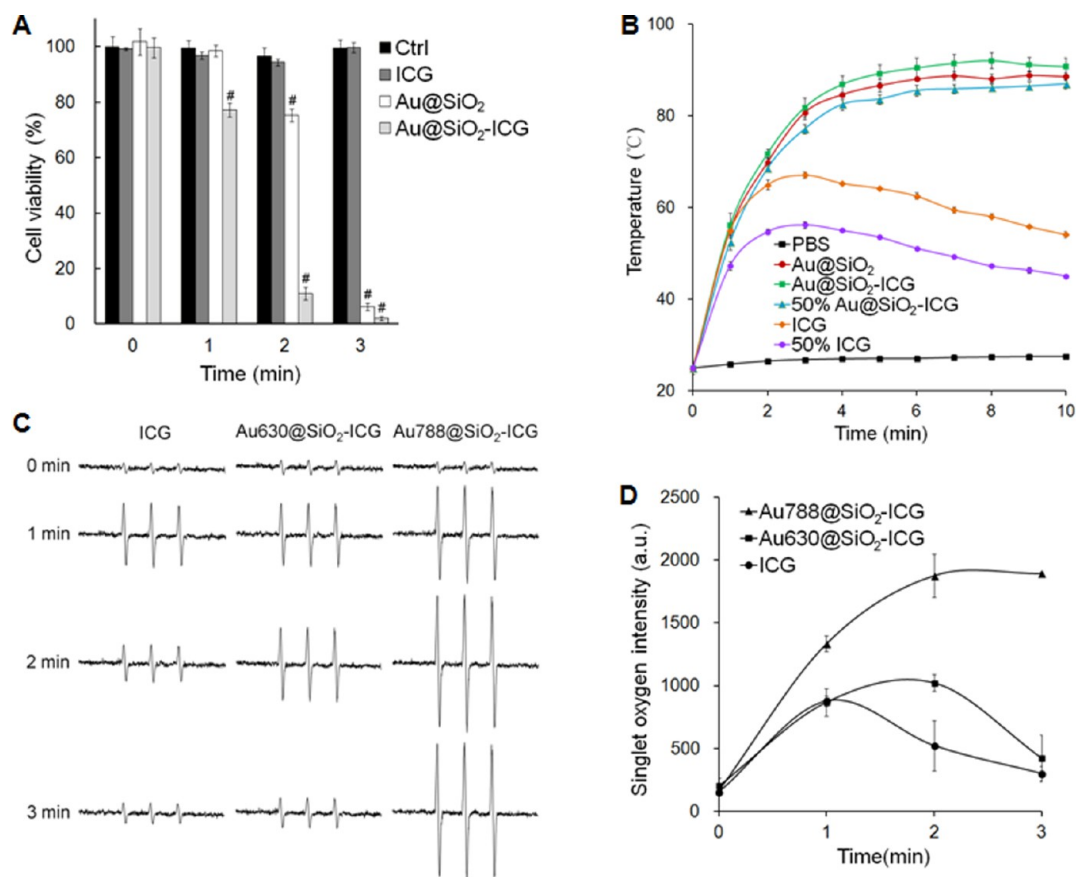
Figure 3. Enhanced PDT of Au@SiO$_2$−ICG *in vitro*. (A) Viability of MDA-MB-231 cells after different treatments and laser irradiation. $^{\#}p < 0.01$ compared to untreated control cells. (B) The photothermal effects of free ICG, Au@SiO$_2$ and Au@SiO$_2$−ICG after laser irradiation. (C) EPR spectra of singlet oxygen after laser irradiation using 2,2,6,6-tetramethyl-4-piperidone (TEMP) as a spin trap. (D) Plot of the intensity of the singlet oxygen signal as a function of irradiation time. The irradiations were carried out under an 8 W/cm^2 power density of 808 nm laser.

Au@SiO$_2$, Au@SiO$_2$−ICG has almost twice the negative surface charges both in deionized water and in DMEM medium (10% fetal bovine serum) (Table S1). Previous studies indicated that the cellular uptake of negatively charged nanoparticles is lower than that of positively charged nanoparticles.[12,43] We, therefore, suggest a similar effect here to explain the difference in cellular uptake. Then, the intracellular NIR fluorescence of ICG was imaged using a confocal fluorescence microscope (Figure 2C). Although the fluorescence increased over time in the cells incubated with both Au@SiO$_2$−ICG and ICG, the former clearly showed stronger and more localized ICG fluorescence owing to the endocytosis of Au@SiO$_2$−ICG, which demonstrates prominent delivery and protection of Au@SiO$_2$ to ICG.

Plasmon-Enhanced PDT of Au@SiO$_2$−ICG *In Vitro*. We next investigated the NIR laser-triggered photothermal and photodynamic tumor cell killing facilitated by Au@SiO$_2$−ICG *in vitro*. MDA-MB-231 cells were incubated with free ICG (30 μM), Au@SiO$_2$ (1 nM) or Au@SiO$_2$−ICG (1 nM Au@SiO$_2$ containing 30 μM ICG) for 24 h in the dark and then irradiated with an 808 nm continuous laser at a power density of 8 W/cm^2 for different times (Figure 3A). Whether there was laser

exposure or not, free ICG did not exhibit obvious cytotoxicity. Au@SiO$_2$ and Au@SiO$_2$−ICG were not toxic when incubated with cells in the dark, but demonstrated time-dependent cytotoxicity when exposed to laser. After 2 min of laser irradiation, Au@SiO$_2$−ICG exhibited significantly stronger phototoxicity than Au@SiO$_2$. After 3 min exposure, however, they exhibited extensive, and similar, cytotoxicity.

In order to interpret the synergistic efficacy of PDT and PTT mediated by Au@SiO$_2$−ICG in more details, the photothermal effects of free ICG, Au@SiO$_2$ and Au@SiO$_2$−ICG were investigated under laser exposure (Figure 3B). On the basis of the quantitative measurements of cellular uptake of Au@SiO$_2$−ICG and Au@SiO$_2$, the uptake amount of Au@SiO$_2$−ICG (about 15% of the treatment amount) is a half of the amount of Au@SiO$_2$ after 24 h incubation (Figure 2B). Therefore, the experimental concentrations were designed in accordance with the intracellular levels of Au@SiO$_2$−ICG (0.15 nM Au@SiO$_2$ containing 4.5 μM ICG) and Au@SiO$_2$ (0.3 nM). During the first 3 min of irradiation, the temperature differences between 0.15 nM Au@SiO$_2$−ICG (Figure 3B, 50% Au@SiO$_2$−ICG) and 0.3 nM Au@SiO$_2$ (Figure 3B, Au@SiO$_2$) are only 2.6, 1.3 and 3.6 °C at each

testing time point, which suggested the similar ability of inducing hyperthermia for PTT. However, $Au@SiO_2$–ICG treated cells demonstrated 77.2 and 11.0% cell viability after 1 and 2 min exposure, much lower than those of $Au@SiO_2$ treated cells (98.4 and 75.3%) (Figure 3A). The significant difference in phototoxicity indicates that the hyperthermia effect is not the main cause of cell death induced by intracellular $Au@SiO_2$–ICG after 1 and 2 min of laser irradiation. In contrast, due to the high temperature upon 3 min laser irradiation, single hyperthermia effect is sufficient for extensive cell killing for both intracellular $Au@SiO_2$ and intracellular $Au@SiO_2$–ICG (Figure 3A). Therefore, we speculate that the enhanced PDT delivered by $Au@SiO_2$–ICG is the primary cause of the cytotoxicity after the first 2 min irradiation, and induces additional cell killing for $Au@SiO_2$–ICG after 3 min laser irradiation.

To explore why the PDT effect of $Au788@SiO_2$–ICG was much greater than that of free ICG, the change of the ICG absorption coefficient following LSPR excitation was detected by employing $Au630@SiO_2$, a control nanoparticle with an LSRP peak at 630 nm, to load ICG (Figure S4A). For comparison, the concentrations of nanoparticles and ICG were kept the same as $Au788@SiO_2$. If the ICG absorption coefficient is not enhanced by a plasmonic effect of $Au788@SiO_2$, the $Au630@SiO_2$–ICG is expected to generate the same ICG-based PDT efficacy as $Au788@SiO_2$–ICG. Using the same cell-incubation and laser irradiation protocols, the enhanced PDT induced by $Au788@SiO_2$–ICG was not reproduced by $Au630@SiO_2$–ICG. The latter showed negligible cytotoxicity in all of the tested groups (Figure S4B). In addition, due to the mismatch between the LSPR peak of $Au630@SiO_2$ and the wavelength of the NIR-laser (808 nm), the photothermal conversion efficiency of $Au630@SiO_2$ is much lower than that of $Au788@SiO_2$. On account of the contribution of incorporated ICG, the temperatures of $Au630@SiO_2$–ICG were all above those of $Au630@SiO_2$ during the whole course of exposure, but below those of free ICG until 6 min (Figure S4C). These results strongly indicate that the overlap between the AuNR LSPR band and the ICG exciton absorption band is crucial to increase the ICG absorption coefficient of $Au@SiO_2$–ICG, and simply intracellular enrichment of ICG by $Au@SiO_2$ is unable to realize greatly improved PDT without the local field enhancement.

$^1O_2$ is a highly reactive oxygen species believed to play a key role in the efficacy of PDT.[4,5] We further compared the production of $^1O_2$ by free ICG, $Au630@SiO_2$–ICG and $Au788@SiO_2$–ICG (the same concentrations of nanoparticle and ICG) under irradiation using electron paramagnetic resonance (EPR) (Figure 3C,D). Exposure to free ICG and $Au630@SiO_2$–ICG resulted in similar $^1O_2$ intensity after 1 min irradiation, and then free ICG-produced $^1O_2$ rapidly decreased due to its poor photostability. $Au630@SiO_2$–ICG maintained its $^1O_2$ signal

intensity up to 2 min, which indicated the single photoprotection of the silica shell. After 3 min exposure, the $Au630@SiO_2$–ICG signal was clearly attenuated. In contrast, $^1O_2$ production by $Au788@SiO_2$–ICG was much higher than that of the other two preparations and signal intensity remained at high even after 3 min exposure. The signal intensity of $Au788@SiO_2$–ICG was 1.5, 3.6, and 6.3 times that of free ICG after 1, 2, and 3 min irradiation, respectively (Figure 3D). However, $Au630@SiO_2$–ICG can only improve the production of ICG for 2 times at most (Figure 3D), that was ineffective for tumor cell killing (Figure S4B). The significant difference in $^1O_2$ intensity between $Au788@SiO_2$–ICG and $Au630@SiO_2$–ICG effectively explains the higher efficiency of $Au@SiO_2$–ICG-mediated enhanced PDT (Figure 3A).

As we expected, the increase in the absorption coefficient of ICG by LEF of the AuNR is a key mechanism to enhance the yield of $^1O_2$. Figure S5 shows the simulated absorbance and scattering features of individual AuNRs (Figure S5A) and distribution of electric field intensity using finite-difference time-domain (FDTD) stimulation (Figure S5B,C,D). The LEF effect decreased progressively from the surface of the AuNR toward the periphery of the silica shell. The incorporated ICG has a suitable spatial location provided by the silica shell to "feel" the LEF effect, and thus its increased absorbance coefficient can strongly enhance the $^1O_2$ yield. Furthermore, the absorbance cross section of the single AuNR is of the order of 10^{-14} m^2 (Figure S5A), which is ~10^6 higher than that of single ICG molecule (~8.7×10^{-20} m^2).[44] This means that if the LSPR band and exciton band overlap, most of irradiated photons at overlap position will be absorbed by the AuNRs. This provides the second protection for the ICG from strong light-induced photobleaching besides the first photoprotection rendered by silica shell. Therefore, more stable and higher $^1O_2$ level was achieved using $Au788@SiO_2$–ICG in comparison with $Au630@SiO_2$–ICG (Figure 3C,D), which neither increased the absorbance coefficient of ICG nor provided the photoprotection of AuNR because of the mismatched LSPR band at 630 nm. Compared with $Au630@SiO_2$–ICG, $Au788@SiO_2$–ICG obtained 1.5, 1.8, and 4.5 folds $^1O_2$ increase after 1, 2, and 3 min irradiation, respectively (Figure 3D). The enhanced photodynamic destruction of MDA-MB-231 cells induced by $Au788@SiO_2$–ICG clearly validated the integrated strategy (Figure 3A, Figure S4B).

Cellular Localization and Stability of $Au@SiO_2$–ICG under Irradiation. To more precisely define the intracellular localization of $Au@SiO_2$–ICG and the morphological changes accompanying laser treatment, MDA-MB-231 cells exposed to free ICG, $Au@SiO_2$ or $Au@SiO_2$–ICG for 24 h in the dark, and then subjected to laser irradiation, were examined by TEM. As shown in Figure 4, in comparison with untreated control cells, which showed no
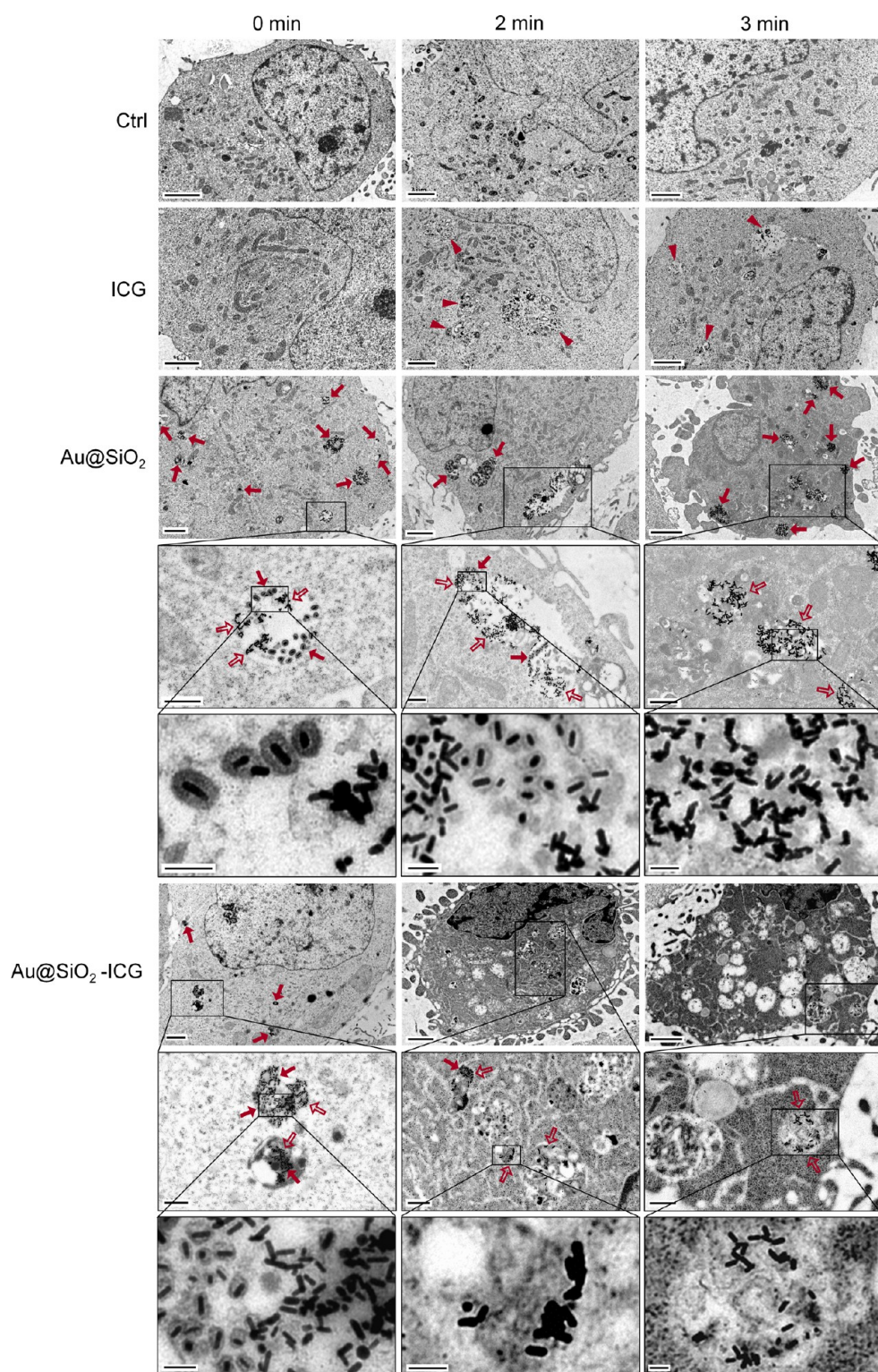
Figure 4. Representative TEM images of MDA-MB-231 cells incubated with free ICG, Au@SiO$_2$ or Au@SiO$_2$—ICG and then treated with laser irradiation (808 nm, 8 W/cm^2). Arrowheads indicate intracellular vesicles induced by irradiated ICG. Solid arrows in frameless images indicate endocytosed nanoparticles. Solid arrows and open arrows in the frame images indicate the nanoparticles with and without an intact silica shell, respectively. Scale bars, 2 μm (frameless images), 500 nm (frame images, the primary amplification) and 100 nm (frame images, the second amplification).

noticeable morphological change after laser exposure, irradiated ICG triggered the marked formation of intracellular vesicles containing internalized cytoplasmic debris, noted as darkly stained granular inclusions (Figure 4, arrowheads in the ICG samples). Most of Au@SiO$_2$ and Au@SiO$_2$—ICG located in cellular vesicles, mainly endosomes and lysosomes (Figure 4, solid arrows in the frameless images), and cell morphology

was not disturbed by either type of nanoparticles without laser exposure. Irradiation led to time-related morphological change in Au@SiO$_2$-treated samples. At the intracellular locations of Au@SiO$_2$, there was swelling and vacuolation of the vesicles after 2 min laser treatment, whereas significant damage, marked by cellular pyknosis, chromatin margination and nuclear fragmentation, occurred after 3 min laser exposure. In contrast, after 2 min laser exposure, striking cell damage was observed in the Au@SiO$_2$-ICG group, with cellular pyknosis, chromatin margination and a large number of empty vacuoles appearing in the cytoplasm. These morphological observations are consistent with the results of cell viability assay (Figure 3A), and visually demonstrate the prominent effects of enhanced PDT mediated by Au@SiO$_2$-ICG.

Many of the observed Au@SiO$_2$ and Au@SiO$_2$-ICG nanoparticles observed retained an intact silica shell on their surface (Figure 4, solid arrows in the framed images), while in some cases only AuNR cores remained (Figure 4, open arrows in the framed images), suggesting possible loss of the SiO$_2$ shell inside the cells. To explore the stabilities of Au@SiO$_2$ and Au@SiO$_2$-ICG and the role of laser irradiation in this process, UV-vis absorbance spectra of Au@SiO$_2$ and Au@SiO$_2$-ICG were obtained before and after irradiation. Au@SiO$_2$ exhibited excellent photostability and its spectrum remained unchanged after laser treatment (Figure S6A). For Au@SiO$_2$-ICG, the LSPR peak showed a slight blue-shift as a result of photodegradation of the loaded-ICG (Figure S6B). These studies indicated that irradiation treatment did not cause obvious shedding of the silica shell *in vitro*. To simulate an intracellular environment, Au@SiO$_2$ and Au@SiO$_2$-ICG were incubated in deionized water or a phagolysosomal simulant fluid in the dark at 37 °C for 24 h, then irradiated for different periods of time. TEM images confirmed that the nanoparticles were stable and no loss of AuNR core or silica thickness was found (Figure S6C,D, Table S2). However, considering the complicacy of intracellular environment, it is possible that some nanoparticles lose their silica shells through the action of intracellular enzymes inside acid vesicles.

It has been shown that Au@SiO$_2$ nanocarriers can trigger their chemotherapeutic drug cargo release through photothermal effect when irradiated with a laser.[16,45] We thus investigated whether Au@SiO$_2$-ICG can release ICG *in vitro* in a controlled way through a photothermal effect. As it is instable in aqueous solution,[39] ICG rapidly degrades *via* thermal decomposition and photodegradation under laser irradiation (Figure S7A,B). This property makes the evaluation of ICG release from its carrier more challenging. To overcome this barrier, a laser dye Rh6G[46] was loaded onto Au@SiO$_2$ as a substitute for ICG in order to study release behavior (Figure S3C). Rh6G exhibits excellent photostability over 3 min laser irradiation (Figure S7C,

D). Under laser exposure, the cumulative release Rh6G from Au@SiO$_2$ was 1.7 times that of the nonirradiated control (Figure S7E), providing support for the proposal that ICG could be released from Au@SiO$_2$ nanocarriers in response to laser treatment. On the basis of this evidence, we speculated that laser triggered release of ICG was also responsible for the slight blue-shift of the LSPR peak of Au@SiO$_2$-ICG in Figure S6B.

Biodistribution of Au@SiO$_2$-ICG *In Vivo*. Distribution of Au@SiO$_2$-ICG *in vivo*, especially in tumor region, was tracked through ICG NIR fluorescence imaging and Au@SiO$_2$-ICG photoacoustic tomography, respectively. Nu/nu mice with orthotopic MDA-MB-231 tumors were injected with saline, free ICG, Au@SiO$_2$ or Au@SiO$_2$-ICG *via* a lateral tail vein. Abdominal fluorescence signals were first recorded at various time points after the injection using a Maestro *in vivo* optical imaging system. As shown in Figure 5A, the ICG fluorescence of Au@SiO$_2$-ICG injected mice gradually increased over time in the tumor region and largely accumulated in the tumor 24 h after administration. The signal remained detectable 48 h after the injection. In contrast, free ICG fluorescence mainly distributed in organs outside the tumor and had disappeared by 24 h after administration. At the 24 and 48 h time points, the tumors and various organs were excised for *ex vivo* imaging to determine the definite distribution of ICG (Figure 5B). After treatment with free ICG, weak fluorescence was visible only in the liver at 24 h, and no signal can be detected at 48 h. Consistent with the result of the whole animal imaging (Figure 5A), Au@SiO$_2$-ICG injection generated a clear signal in the tumor at both the 24 and 48 h time points. In addition, signals of varying intensity were also observed in the liver, kidney and lung after the treatment of Au@SiO$_2$-ICG. These imaging results illustrated that Au@SiO$_2$ greatly increase the stability of ICG in the circulation and promote the selective accumulation of ICG in tumors.

To confirm the tumor accumulation of Au@SiO$_2$-ICG, fast multispectral optoacoustic tomography (MSOT) was used to achieve the high resolution optical imaging of longitudinal sections of mice.[47,48] Figure 5C presents representative MSOT images of nu/nu mice with orthotopic MDA-MB-231 tumors following the administration of Au@SiO$_2$-ICG, Au@SiO$_2$ or free ICG. Although some signals from free ICG was found arroud the tumor region, there was little signal from the tumor itself, and the signal was quickly diminished over time. In contrast, the signals of both Au@SiO$_2$-ICG and Au@SiO$_2$ gradually increased over time in the tumor regions by 24 h, and remained detectable 48 h after the administration. The optoacoustic signals of Au@SiO$_2$-ICG (Figure 5C) corresponded well to its ICG fluorescence signals (Figure 5A) at both 24 and 48 h time points, that further evidenced the significant accumulation of Au@SiO$_2$-ICG in the tumor regions
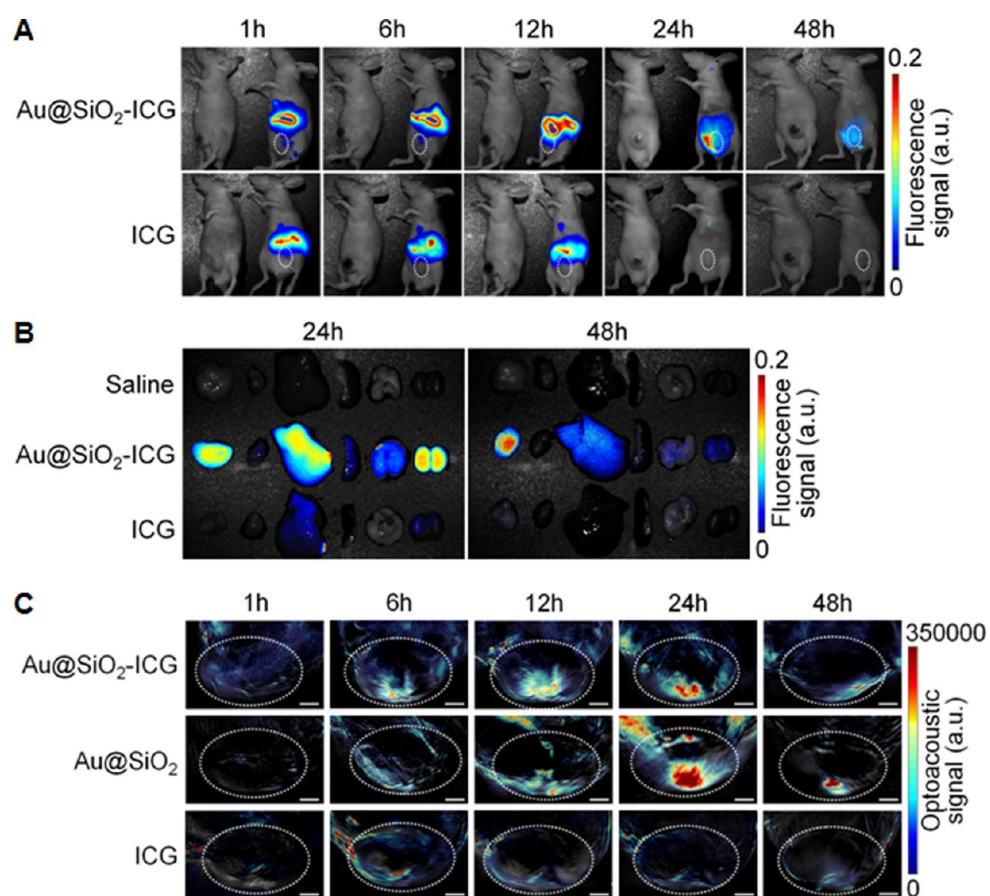
Figure 5. Distribution of Au@SiO$_2$−ICG following intravenous administration to tumor-bearing mice. (A) Real-time NIR fluorescence images after intravenous injection of Au@SiO$_2$−ICG and ICG into nu/nu mice. The white dashed circles indicate the location of the tumor. (B) *Ex vivo* **images of mice tissues (from left to right: tumor, heart, liver, spleen, lung, kidney). (C) MSOT of Au@SiO$_2$−ICG, Au@SiO$_2$ and free ICG at 800 nm on longitudinal section of orthotopic breast tumor regions at 24 h. The white dashed circles highlight the tumor regions. Scale bars, 2 mm.**

and provided necessary prerequisite for subsequent PDT and PTT *in vivo*.

Antitumor Efficacy of Au@SiO$_2$−ICG *In Vivo*. To investigate the antitumor efficacy of Au@SiO$_2$−ICG-based PTT/PDT *in vivo*, the photothermal effect of Au@SiO$_2$−ICG was monitored through an infrared thermal imaging camera. At 24 h postinjection, orthotopic MDA-MB-231 tumors in nu/nu mice were exposed to an 808 nm laser (Figure 6A). Although Au@SiO$_2$−ICG has excellent photothermal conversion efficiency to generate very high temperature with a short laser exposure *in vitro* (Figure 3B), far milder temperature is preferred in conventional clinical thermal therapy.[49] To ensure that the tumor temperature reach the threshold needed to induce irreversible tumor damage, and to guarantee the safety of the treatment to healthy tissues, a very low power density of 1.4 W/cm^2 was applied and the laser irradiation time was limited to 3 min to make sure that the tumor surface temperature was no more than 45 °C.[28] The photothermal conversion efficiency of Au@SiO$_2$−ICG with this mild treatment was also confirmed *in vitro* (Figure S8). *In vivo*, the tumor surface temperatures of Au@SiO$_2$ and Au@SiO$_2$−ICG injected mice were 43.4 and 45.0 °C following a short irradiation

of 3 min. A moderate increase in tumor temperature (4.2 °C) was observed in free ICG-injected mice, while the tumor in mice injected with saline only increased by 2.6 °C. Temperatures in all groups quickly declined to the body temperature after a 1 min interval, suggesting that the treatment is likely to be safe.

To evaluate the antitumor effects of Au@SiO$_2$−ICG treatment, nu/nu mice bearing with orthotopic MDA-MB-231 tumors were injected with Au@SiO$_2$−ICG (Au@SiO$_2$, 10 mg/kg; ICG, 1.15 mg/kg) and related control preparations into a tail vein. The tumor region was then irradiated with an 808 nm laser 24 h after the injection. To avoid possible tissue damage by hyperthermia, the laser treatment was carried out for a total of 12 min at a power density of 1.4 W/cm^2 with a 1 min interval after every 3 min of exposure. Mice were conscious and the epidermis was not burnt during the laser process. Irradiation was carried out on three occasions (1, 8, and 15 days) during the 30 days of the experiment (Figure 6B). Tumor growth was relatively rapid in both the saline and saline/irradiation groups, indicating that simple thermal therapy with current laser treatment is ineffective at inhibiting tumor growth. ICG or Au@SiO$_2$ coupled with laser
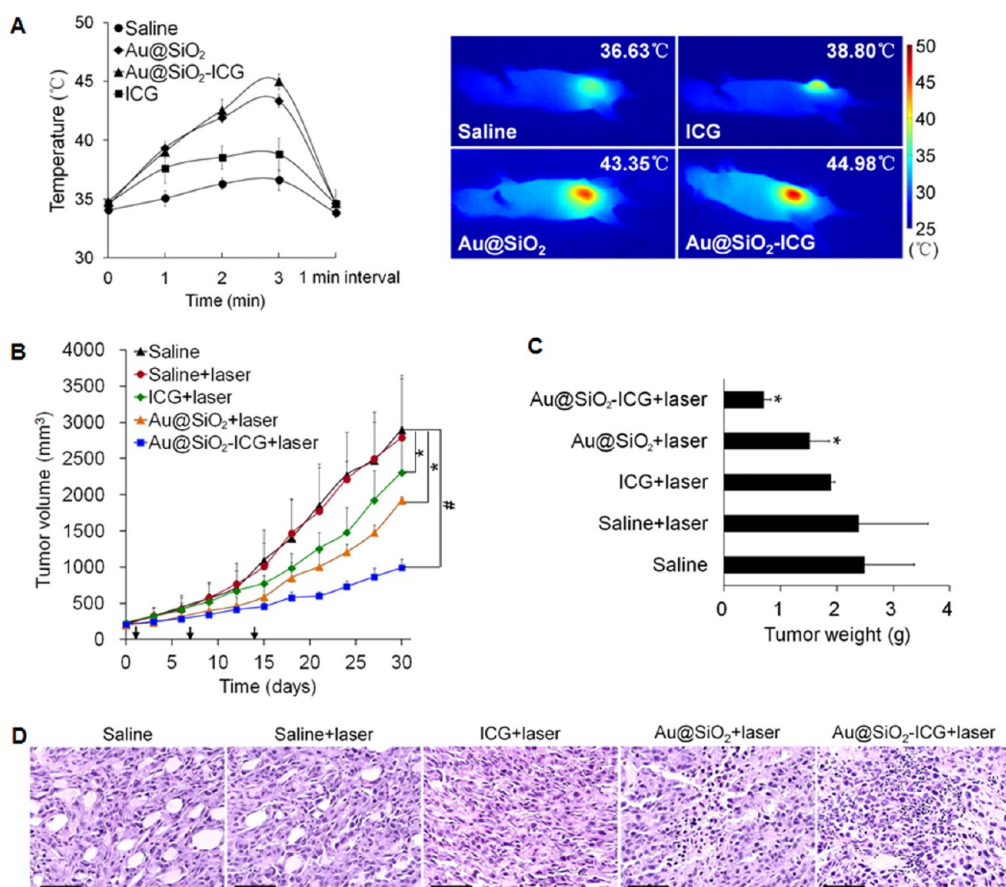
Figure 6. Antitumor activity of Au@SiO$_2$−ICG *in vivo*. (A) Heating curve (left) and infrared thermal images (right, at the 3 min time point) of orthotopic breast tumors in nu/nu mice after irradiation with an 808 nm NIR laser 24 h after intravenous injection of Au@SiO$_2$−ICG and various control reagents. (B) Tumor growth in nu/nu mice after various treatments and laser irradiation. *p < 0.05, #p < 0.01 (n = 5). The arrows indicate when laser treatments were carried out. (C) Tumor weight in the various treatment groups on day 30. *p < 0.05 (n = 5) compared to the saline group. (D) Representative H&E sections of the tumors after treatment for 30 days. Scale bars, 20 μm.

irradiation hindered tumor growth to a certain extent, demonstrating the therapeutic efficacy of single ICG-based PDT or Au@SiO$_2$-based PTT respectively. However, a strong synergistic effect of PDT and PTT in inhibiting tumor growth was displayed when mice injected with Au@SiO$_2$−ICG were subjected to laser exposure. At the end of the 30 day treatments, the mice were sacrificed and the tumors excised and weighed (Figure 6C). The average tumor weight in the Au@-SiO$_2$−ICG/irradiation group was lower than those of Au@SiO$_2$/irradiation group and ICG/irradiation groups. These results are consistent to the result of tumor growth. H&E staining of tumor sections collected from the treated mice at day 30 showed that most tumor cells in the Au@SiO$_2$−ICG/irradiation group had been destroyed (Figure 6D). Prominent inflammatory cell infiltration was also evident. Some cell damage was seen in tumors in the Au@SiO$_2$/irradiation group, in contrast to the saline and ICG control groups where no obvious tumor cell damage was observed.

The antitumor efficacy of Au@SiO$_2$−ICG-based laser treatment was much more than the sum of those of single ICG-based PDT and single Au@SiO$_2$-based PTT.

After 30 day treatments, the average tumor volume of Au@SiO$_2$−ICG/irradiation group, Au@SiO$_2$/irradiation group and ICG/irradiation group decreased 65.9, 33.7 and 20.4%, respectively (Figure 6B), and the average tumor weight in above groups was 71.7, 39.2 and 24.0% lower than that of the saline control mice, respectively (Figure 6C). Similarly, total destroyed cells in the H&E staining images of ICG/irradiation group and Au@SiO$_2$/irradiation group were less than that of Au@SiO$_2$−ICG/irradiation group (Figure 6D). In addition, consistent with the result *in vitro* (Figure 3A), simply laser-triggered hyperthermia induced by Au@SiO$_2$ is more effective in antitumor therapy than simply ICG-based PDT *in vivo* (Figure 6B,C), although the mild laser treatment (1.4 W/cm^2, 3 min) had very limited antitumor effect in both treatment modalities. This is closely related to the distribution of ICG and Au@SiO$_2$ in tumors (Figure 5). All these results clearly demonstrated the synergistic antitumor effects of Au@SiO$_2$−ICG *in vivo*.

CONCLUSIONS

We have successfully designed and validated a novel plasmon-enhanced PDT for breast tumor by fabricating

a nanoplatform composed of mesoporous silica-coated AuNRs incorporating ICG. The LSPR peak of the AuNR core has been regulated to overlap with the exciton band of ICG, thus increasing the absorption coefficient of incorporated ICG by virtue of the LEF effect. Such overlap also helps protect the loaded ICG from photodegradation based on $\sim 10^6$ higher absorbance cross section of the AuNR. In addition, the formation of ICG aggregate facilitated by SiO_2 enhances photostability of incorporated ICG as well. The AuNR@SiO_2—ICG formulation dramatically increases singlet oxygen generation under laser excitation, relative to free ICG, and demonstrates enhanced photodynamic destruction of human breast carcinoma cell MDA-MB-231. In addition, cellular uptake and retaining of ICG in the tumor regions is enhanced due to the stabilization and delivery of ICG provided by AuNR@SiO_2 nanocarrier. This was confirmed by three imaging modes (NIR fluorescence, two-photon luminescence and photoacoustic tomography) both *in vitro* and *in vivo*. Mild photothermal heating at a very low laser power density was sufficient to ensure that AuNR@SiO_2—ICG induced a clear inhibition of orthotopic tumor growth through the synergistic effect of PTT and PDT. Our study highlights a general design principle for enhancing the effectiveness of photosensitizers based on plasmon enhancement and protection, which holds great promises for cancer therapy by further development.

METHODS

Materials. Sodium borohydride ($NaBH_4$), chlorauric acid ($HAuCl_4 \cdot 3H_2O$), cetyltrimethylammonium bromide (CTAB), sodium citrate, silver nitrate ($AgNO_3$), and L-ascorbic acid (AA), were purchased from Alfa Aesar (Ward Hill, USA) and used as received. Sodium hydroxide (NaOH), sulfuric acid (H_2SO_4), and tetraethyl orthosilicate (TEOS), were at least analytical reagent grade and were purchased from Beijing Chemical Reagent Company (Beijing, China). Indocyanine green (ICG) was purchased from Sigma-Aldrich (St. Louis, USA). Cell Counting Kit-8 (CCK-8) was purchased from Dojindo Molecular Technologies (Kumamoto Techno, Japan). A human breast carcinoma cell line MDA-MB-231 was obtained from the American Type Culture Collection (ATCC, Manassas, USA). All solutions were prepared using ultrapure water (Milli Q-plus system, Millipore, Billerica, USA) with a resistivity of 18.2 MΩ·cm.

Synthesis of AuNR. AuNRs were synthesized using the well-developed seed-mediated growth method. Briefly, CTAB-capped Au seeds were synthesized by chemical reduction of $HAuCl_4$ with $NaBH_4$: CTAB (7.5 mL, 0.1 M) was mixed with $HAuCl_4$ (100 μL, 25 mM) and diluted with water to 9.4 mL. Then, ice-cold $NaBH_4$ (0.6 mL, 0.01 M) was added with stirring. The solution immediately turned from bright yellow to brown, indicating the formation of Au seeds. The Au seeds were used within 2—5 h. For a typical preparation of the AuNRs, in a growth solution consisting of a mixture of CTAB (100 mL, 0.1 M), $HAuCl_4$ (2 mL, 25 mM), $AgNO_3$ (100 μL, 0.1 M), H_2SO_4 (1 mL, 1 M), and AA (800 μL, 0.1 M), 240 μL of seed solution was added to initiate the growth of the AuNRs. The incubation was carried out at 30 °C for 12 h.

Preparation of Au@SiO_2 and Au@SiO_2—ICG. Mesoporous silica coating of AuNRs was carried out according to the method of Gorelikov and Matsuura with some modifications.[38] The as-synthesized AuNRs were washed by centrifugation (60 mL aliquots at a time, at 9200 rpm for 12 min). The pellet was suspended in 60 mL of water, and 200 μL of 0.2 M NaOH solution was added with stirring. Three 60 μL aliquots of 20% TEOS in ethanol were subsequently added under gentle stirring at 30 min intervals. The mixture was incubated for 2 days at 30 °C. The samples were purified by centrifuging the solution at 9500 rpm for 20 min then washing three times in ethanol.

Au@SiO_2—ICG was obtained by simply sonication (95 W) of a mixture (mase ratio, 6:1) of Au@SiO_2 and ICG for 15 min in an ice bath, and the product was washed three times with water by centrifuging (9200 rpm for 12 min). The amount of ICG loaded onto Au@SiO_2 was determined using a UV—vis spectrophotometer at 780 nm. The ICG loading content was calculated by the following equation: Loading capacity = (weight of loaded ICG)/(weight of Au@SiO_2—ICG). The preparation of Au@SiO_2—Rh6G was carried out using exactly the same method, with the exception that the loading content of Rh6G was determined using a UV—vis spectrophotometer at 525 nm.

Characterization. Transmission electron microscopy (TEM) images were obtained with a Tecnai G^2 20 S-TWIN TEM operating at an acceleration voltage of 200 kV. Elemental analysis was performed with energy-dispersive X-ray (EDX) from TEM. UV—vis—NIR absorption spectra were recorded on a Varian Cary 50. The hydrodynamic diameter and zeta potential of the samples were measured on a DelsaNanoC dynamic light scattering particle analyzer. Fluorescence spectra were acquired on a Hitachi F-4600.

Cell Culture. MDA-MB-231 cells was maintained at 37 °C (5% CO_2) in DMEM supplemented with 10% (v/v) fetal bovine serum, 2 mM L-glutamine, 20 mM HEPES, 100 U/mL penicillin and 1 mg/mL streptomycin.

Confocal Microscopy. Cells were seeded onto a 35 mm borosilicate, chambered cover glass (Nunc, USA) at a density of 1×10^5 cells/mL, and incubated with Au@SiO_2—ICG, Au@SiO_2 or free ICG in the dark at 37 °C for 24 h. Confocal fluorescence microscopy images of cellular ICG were acquired with a Nikon Ti-e microscope equipped with an UltraVIEW Vox confocal attachment (PerkinElmer) with an excitation wavelength of 633 nm. Two-photo luminescence images of Au@SiO_2 and Au@SiO_2—ICG within cells were obtained using a confocal microscope (Olympus FV 1000) equipped with a femto-second Ti:sapphire laser (Spectra-physics Mai Tai DeepSee) with excitation at 800 nm and emission at 520—560 nm.

ICP-MS. Cells exposed for 24 h to Au@SiO_2 or Au@SiO_2—ICG at 37 °C were washed and counted. For each sample, 1×10^7 cells were collected for ICP-MS analysis (NexION 300X, Perkinelmer). Prior to elemental analysis, the samples were predigested overnight in a mixture of HNO_3 and HCl (3 mL, 3:1, w/w) and then coincubated with H_2O_2 (2 mL 30%, w/w) at 150 °C for 3 h.[16] After the solution volume was adjusted to 3 mL using the HNO_3 and HCl mixture, the Au content was analyzed using ICP-MS. Bismuth (10 ng/mL) was chosen as an internal standard.

Cell Viability. Cells were seeded into 96-well plates at a density of 5×10^4 cells/mL in the presence of free ICG, Au@SiO_2 or Au@SiO_2—ICG (Au@SiO_2, 1 nM; ICG, 30 μM) at 37 °C. After treatment for 24 h in the dark, the cells were irradiated with an 808 nm continuous-wave diode laser (Daheng Science & Technology, China) at a power density of 8 W/cm^2 (power, 1 W; diameter of the laser spots, 4 mm) for various times. After irradiation, the medium was replaced with fresh medium and the cells cultured for a further 24 h. The proportion of viable cells was evaluated using a CCK-8 assay.[50]

Photothermal Effects *In Vitro*. The aqueous solutions (200 μL) of free ICG (9 μM or 4.5 μM), Au@SiO_2 (0.3 nM) and Au@SiO_2—ICG (0.3 nM Au@SiO_2 containing 9 μM ICG or 0.15 nM Au@SiO_2 containing 4.5 μM ICG) were irradiated with an 808 nm continuous laser at a power density of 8 W/cm^2 for 10 min. The temperature was monitored every minute by a thermocouple. Each test was repeated 3 times.

EPR. Solutions of free ICG, Au@SiO_2 and Au@SiO_2—ICG (Au@SiO_2, 1 nM; ICG, 30 μM) were irradiated with an 808 nm

continuous laser at a power density of 8 W/cm^2 for 3 min. Singlet oxygen levels were detected by the EPR trapping technique using 2,2,6,6-tetramethyl-4-piperidone (TEMP) as a spin trap.[51] The EPR spectra were recorded on a Bruker ESP300E spectrometer operating at the X-band.

FDTD Simulation. FDTD simulations were performed using FDTD Solutions 8.6, which was developed by Lumerical Solutions, Inc. During the simulations, an electromagnetic pulse in the wavelength range 600−900 nm was launched into a box containing the target nanostructure. A mesh size of 0.5 nm was used to calculate the LSPR peak and electric field enhancements of the Au nanorod and the Au@SiO$_2$ core−shell structure. The refractive index of the surrounding medium was set to be 1.33, which is the index of water. The dielectric functions of Au and SiO$_2$ were obtained from Johnson, and Christy and Palik, respectively.[52] The sizes of the nanostructures were set according to the average sizes measured from the TEM images. The Au nanorods were modeled as a cylinder with two hemispheres at each end. To better mimic the mesoporous structure of the SiO$_2$ shell, we added some channels inside the shell, which also connected to the surrounding. The diameter and total length of the Au nanorod were 14.4 and 49 nm, respectively. The shell thickness was set at 17.6 nm. The channels were represented by flat discs with a thickness of 3 nm. There were 19 flat discs parallel to the transverse axis of the Au nanorod and 6 flat discs parallel to the longitudinal axis. The porous density was controlled at 87.8%.

TEM Imaging of Cells. Cells were seeded into 100 mm plates at a density of 1×10^6 cells/mL and were incubated with free ICG, Au@SiO$_2$ or Au@SiO$_2$−ICG (Au@SiO$_2$, 1 nM; ICG, 30 μM) in the dark at 37 °C for 24 h. Then the cells were washed and exposed to an 808 nm continuous laser at a power density of 8 W/cm^2 for various times. After irradiation, the medium was replaced and culture continued for a further 24 h. The cells were collected by centrifugation, then immediately fixed overnight at 4 °C in 2.5% (w/w) glutaraldehyde. Samples were prepared for TEM according to standard procedures then viewed using a JEOL JEM-1400 electron microscope (Japan).

***In Vitro* Drug Release.** Au@SiO$_2$−Rh6G in PBS (pH 7.4) was irradiated with an 808 nm continuous laser at a power density of 8 W/cm^2 for 3 min and then agitated at 37 °C for 56 h. Au@SiO$_2$−Rh6G without irradiation was used as negative control. At 1 h interval, aliquots were withdrawn and centrifuged to pellet the nanoparticles. The amount of released Rh6G in the supernatant was measured by a UV−vis spectrophotometer at 525 nm.

Tumor Xenografts and Antitumor Therapy. Orthotopic breast tumor xenografts were implanted into female BALB/c nude mice by injecting 5×10^6 MDA-MB-231 cells into the mammary fat pad (5 mice/group). When tumor diameters reached 5−6 mm, free ICG, Au@SiO$_2$ or Au@SiO$_2$−ICG (Au@SiO$_2$, 10 mg/kg; ICG, 1.15 mg/kg) was injected through the tail vein on days 1, 8, and 15. The tumor region was irradiated with an 808 nm laser 24 h after each injection. To avoid possible tissue damage by hyperthermia, the laser treatment was carried out for 12 min at a power density of 1.4 W/cm^2 (power, 0.7 W; the diameter of the laser spot, 8 mm) with 1 min interval after every 3 min of the exposure. Mice were conscious and the epidermis was not burnt during the laser process. Tumor size was measured using digital vernier calipers every day. The tumor volumes were determined by the following formula: Volume = (tumor length) × (tumor width)^2/2. On day 30, the mice were sacrificed and the tumors were excised and weighed. Tumor sections were further investigated after H&E staining.

***In Vivo* Imaging.** Nu/nu mice with orthotopic MDA-MB-231 tumors were injected by a lateral tail vein with saline, free ICG, Au@SiO$_2$ or Au@SiO$_2$−ICG (Au@SiO$_2$, 10 mg/kg; ICG, 1.15 mg/kg). Real-time NIR fluorescent images of ICG in mice were recorded at various time points after the injection with a Maestro *in vivo* spectrum imaging system (Cri, Woburn, MA, USA) at an excitation wavelength of 735 nm and an emission wavelength of 780−950 nm. The mice were sacrificed 24 and 48 h after the injection and the tumors, hearts, livers, kidneys, lungs and spleens were analyzed for *ex vivo* fluorescence. Infrared thermal images of tumors were obtained using an infrared thermal imaging camera (FLIR S60, USA) under irradiation with an 808 nm laser at a power density of 1.4 W/cm^2 24 h post intravenous injection.

MSOT. A real-time MSOT scanner was utilized in this study (MSOT inVision 128, iThera medical, Germany). Tumor-bearing mice were anesthetized with isoflurane, and placed in supine position in an animal holder. Cross-sectional multispectral optoacoustic image data sets were acquired through the tumor at different wavelengths in the NIR window (from 680 to 900 nm, at 10 nm intervals). Reconstruction of single wavelength optoacoustic images was carried out using the interpolated matrix model inversion method.[53]

Statistical Analysis. All experiments were performed in triplicate unless otherwise indicated. Results were expressed as means ± standard deviation. ANOVA was used for statistical analysis. A probability level of 95% ($p < 0.05$) was considered to be significantly different.

Conflict of Interest: The authors declare no competing financial interest.

Supporting Information Available: Structure of ICG; Adsorption saturation of Au@SiO$_2$−ICG; Fluorescence quenching of Rh6G in Au@SiO$_2$; Zeta potential of Au@SiO$_2$ and Au@SiO$_2$−ICG; Tumor cell-killing effect of Au630@SiO$_2$−ICG; LEF-enhanced PDT in Au778@SiO$_2$−ICG; Stability of Au@SiO$_2$ and Au@SiO$_2$−ICG under laser irradiation; Variation of nanoparticle sizes after laser irradiation; Laser-induced photosensitizer release from AuSiO$_2$; The photothermal effects of free ICG, Au@SiO$_2$ and Au@SiO$_2$−ICG after laser irradiation (808 nm, 1.4 W/cm^2). This material is available free of charge *via* the Internet at http://pubs.acs.org.

REFERENCES AND NOTES

1. Menon, J. U.; Jadeja, P.; Tambe, P.; Vu, K.; Yuan, B.; Nguyen, K. T. Nanomaterials for Photo-Based Diagnostic and Therapeutic Applications. *Theranostics* **2013**, *3*, 152–166.

2. Rai, P.; Mallidi, S.; Zheng, X.; Rahmanzadeh, R.; Mir, Y.; Elrington, S.; Khurshid, A.; Hasan, T. Development and Applications of Photo-Triggered Theranostic Agents. *Adv. Drug Delivery Rev.* **2010**, *62*, 1094–1124.

3. Yong, Y.; Zhou, L.; Gu, Z.; Yan, L.; Tian, G.; Zheng, X.; Liu, X.; Zhang, X.; Shi, J.; Cong, W.; *et al.* WS$_2$ Nanosheet as a New Photosensitizer Carrier for Combined Photodynamic and Photothermal Therapy of Cancer Cells. *Nanoscale* **2014**, *6*, 10394–103403.

4. Castano, A. P.; Mroz, P.; Hamblin, M. R. Photodynamic Therapy and Anti-tumour Immunity. *Nat. Rev. Cancer* **2006**, *6*, 535–545.

5. Dolmans, D. E.; Fukumura, D.; Jain, R. K. Photodynamic Therapy for Cancer. *Nat. Rev. Cancer* **2003**, *3*, 380–387.

6. Zhang, Y.; Aslan, K.; Previte, M. J.; Geddes, C. D. Metal-Enhanced Singlet Oxygen Generation: a Consequence of Plasmon Enhanced Triplet Yields. *J. Fluoresc.* **2007**, *17*, 345–349.

7. Zhang, Y.; Aslan, K.; Previte, M. J.; Geddes, C. D. Plasmonic Engineering of Singlet Oxygen Generation. *Proc. Natl. Acad. Sci. U. S. A.* **2008**, *105*, 1798–1802.

8. Karolin, J.; Geddes, C. D. Metal-Enhanced Fluorescence Based Excitation Volumetric Effect of Plasmon-Enhanced Singlet Oxygen and Super Oxide Generation. *Phys. Chem. Chem. Phys.* **2013**, *15*, 15740–15745.

9. Kochuveedu, S. T.; Kim, D. H. Surface Plasmon Resonance Mediated Photoluminescence Properties of Nanostructured Multicomponent Fluorophore Systems. *Nanoscale* **2014**, *6*, 4966–4984.

10. Eustis, S.; el-Sayed, M. A. Why Gold Nanoparticles are More Precious than Pretty Gold: Noble Metal Surface Plasmon

Resonance and its Enhancement of The Radiative and Nonradiative Properties of Nanocrystals of Different Shapes. *Chem. Soc. Rev.* **2006**, *35*, 209–217.

11. Zhang, Z.; Wang, J.; Chen, C. Gold Nanorods Based Platforms for Light-Mediated Theranostics. *Theranostics* **2013**, *3*, 223.

12. Dreaden, E. C.; Alkilany, A. M.; Huang, X.; Murphy, C. J.; El-Sayed, M. A. The Golden Age: Gold Nanoparticles for Biomedicine. *Chem. Soc. Rev.* **2012**, *41*, 2740–2779.

13. Qin, Z.; Bischof, J. C. Thermophysical and Biological Responses of Gold Nanoparticle Laser Heating. *Chem. Soc. Rev.* **2012**, *41*, 1191–1217.

14. Zhang, Z.; Wang, L.; Wang, J.; Jiang, X.; Li, X.; Hu, Z.; Ji, Y.; Wu, X.; Chen, C. Mesoporous Silica-Coated Gold Nanorods as a Light-Mediated Multifunctional Theranostic Platform for Cancer Treatment. *Adv. Mater.* **2012**, *24*, 1418–1423.

15. Fan, Z.; Shelton, M.; Singh, A. K.; Senapati, D.; Khan, S. A.; Ray, P. C. Multifunctional Plasmonic Shell-Magnetic Core Nanoparticles for Targeted Diagnostics, Isolation, and Photothermal Destruction of Tumor Cells. *ACS Nano* **2012**, *6*, 1065–1073.

16. Wang, L.; Lin, X.; Wang, J.; Hu, Z.; Ji, Y.; Hou, S.; Zhao, Y.; Wu, X.; Chen, C. Novel Insights into Combating Cancer Chemotherapy Resistance Using a Plasmonic Nanocarrier: Enhancing Drug Sensitiveness and Accumulation Simultaneously with Localized Mild Photothermal Stimulus of Femtosecond Pulsed Laser. *Adv. Funct. Mater.* **2014**, 10.1002/adfm.201400015.

17. Liu, H.; Liu, T.; Wu, X.; Li, L.; Tan, L.; Chen, D.; Tang, F. Targeting Gold Nanoshells on Silica Nanorattles: a Drug Cocktail to Fight Breast Tumors *via* a Single Irradiation with Near-Infrared Laser Light. *Adv. Mater.* **2012**, *24*, 755–761.

18. Topete, A.; Alatorre-Meda, M.; Iglesias, P.; Villar-Alvarez, E. M.; Barbosa, S.; Costoya, J. A.; Taboada, P.; Mosquera, V. Fluorescent Drug-Loaded, Polymeric-Based, Branched Gold Nanoshells for Localized Multimodal Therapy and Imaging of Tumoral Cells. *ACS Nano* **2014**, *8*, 2725–2738.

19. Zhang, Y.; Qian, J.; Wang, D.; Wang, Y.; He, S. Multifunctional Gold Nanorods with Ultrahigh Stability and Tunability for *In Vivo* Fluorescence Imaging, SERS Detection, and Photodynamic Therapy. *Angew. Chem., Int. Ed. Engl.* **2013**, *52*, 1148–1151.

20. Wang, S.; Huang, P.; Nie, L.; Xing, R.; Liu, D.; Wang, Z.; Lin, J.; Chen, S.; Niu, G.; Lu, G. Single Continuous Wave Laser Induced Photodynamic/Plasmonic Photothermal Therapy Using Photosensitizer-Functionalized Gold Nanostars. *Adv. Mater.* **2013**, *25*, 3055–3061.

21. Wang, J.; Zhu, G.; You, M.; Song, E.; Shukoor, M. I.; Zhang, K.; Altman, M. B.; Chen, Y.; Zhu, Z.; Huang, C. Z. Assembly of Aptamer Switch Probes and Photosensitizer on Gold Nanorods for Targeted Photothermal and Photodynamic Cancer Therapy. *ACS Nano* **2012**, *6*, 5070–5077.

22. Chen, R.; Wang, X.; Yao, X.; Zheng, X.; Wang, J.; Jiang, X. Near-IR-Triggered Photothermal/Photodynamic Dual-Modality Therapy System *via* Chitosan Hybrid Nanospheres. *Biomaterials* **2013**, *34*, 8314–8322.

23. Khaing, O. M. K.; Yang, Y.; Hu, Y.; Gomez, M.; Du, H.; Wang, H. Gold Nanoparticle-Enhanced and Size-Dependent Generation of Reactive Oxygen Species from Protoporphyrin IX. *ACS Nano* **2012**, *6*, 1939–1947.

24. Chu, Z.; Yin, C.; Zhang, S.; Lin, G.; Li, Q. Surface Plasmon Enhanced Drug Efficacy Using Core−Shell Au@SiO$_2$ Nanoparticle Carrier. *Nanoscale* **2013**, *5*, 3406–3411.

25. Landsman, M. L.; Kwant, G.; Mook, G. A.; Zijlstra, W. G. Light-Absorbing Properties, Stability, and Spectral Stabilization of Indocyanine Green. *J. Appl. Physiol.* **1976**, *40*, 575–583.

26. Desmettre, T.; Devoisselle, J.; Mordon, S. Fluorescence Properties and Metabolic Features of Indocyanine Green (ICG) as Related to Angiography. *Surv. Ophthalmol.* **2000**, *45*, 15–27.

27. Luo, S.; Zhang, E.; Su, Y.; Cheng, T.; Shi, C. A Review of NIR Dyes in Cancer Targeting and Imaging. *Biomaterials* **2011**, *32*, 7127–7138.

28. Zheng, M.; Yue, C.; Ma, Y.; Gong, P.; Zhao, P.; Zheng, C.; Sheng, Z.; Zhang, P.; Wang, Z.; Cai, L. Single-Step Assembly of DOX/ICG Loaded Lipid-Polymer Nanoparticles for Highly Effective Chemo-photothermal Combination Therapy. *ACS Nano* **2013**, *7*, 2056–2067.

29. Zheng, X.; Zhou, F.; Wu, B.; Chen, W. R.; Xing, D. Enhanced Tumor Treatment Using Biofunctional Indocyanine Green-Containing Nanostructure by Intratumoral or Intravenous Injection. *Mol. Pharmaceutics* **2012**, *9*, 514–522.

30. Kuo, W.-S.; Chang, Y.-T.; Cho, K.-C.; Chiu, K.-C.; Lien, C.-H.; Yeh, C.-S.; Chen, S.-J. Gold Nanomaterials Conjugated with Indocyanine Green for Dual-Modality Photodynamic and Photothermal Therapy. *Biomaterials* **2012**, *33*, 3270–3278.

31. Zheng, X.; Xing, D.; Zhou, F.; Wu, B.; Chen, W. R. Indocyanine Green-Containing Nanostructure as Near Infrared Dual-Functional Targeting Probes for Optical Imaging and Photothermal Therapy. *Mol. Pharmaceutics* **2011**, *8*, 447–456.

32. Barth, B. M.; E, I. A.; Shanmugavelandy, S. S.; Kaiser, J. M.; Crespo-Gonzalez, D.; DiVittore, N. A.; McGovern, C.; Goff, T. M.; Keasey, N. R.; Adair, J. H.; *et al.* Targeted Indocyanine-Green-Loaded Calcium Phosphosilicate Nanoparticles for *In Vivo* Photodynamic Therapy of Leukemia. *ACS Nano* **2011**, *5*, 5325–5337.

33. Daniele, M. A.; Shaughnessy, M. L.; Roeder, R.; Childress, A.; Bandera, Y. P.; Foulger, S. Magnetic Nanoclusters Exhibiting Protein-Activated Near-Infrared Fluorescence. *ACS Nano* **2013**, *7*, 203–213.

34. Zheng, C.; Zheng, M.; Gong, P.; Jia, D.; Zhang, P.; Shi, B.; Sheng, Z.; Ma, Y.; Cai, L. Indocyanine Green-Loaded Biodegradable Tumor Targeting Nanoprobes for *In Vitro* and *In Vivo* Imaging. *Biomaterials* **2012**, *33*, 5603–5609.

35. Kuo, W. S.; Chang, C. N.; Chang, Y. T.; Yang, M. H.; Chien, Y. H.; Chen, S. J.; Yeh, C. S. Gold Nanorods in Photodynamic Therapy, as Hyperthermia Agents, and in Near-Infrared Optical Imaging. *Angew. Chem., Int. Ed. Engl.* **2010**, *49*, 2711–2715.

36. Holzer, W.; Mauerer, M.; Penzkofer, A.; Szeimies, R. M.; Abels, C.; Landthaler, M.; Baumler, W. Photostability and Thermal Stability of Indocyanine Green. *J. Photochem. Photobiol., B* **1998**, *47*, 155–164.

37. Lee, C.-H.; Cheng, S.-H.; Wang, Y.; Chen, Y.-C.; Chen, N.-T.; Souris, J.; Chen, C.-T.; Mou, C.-Y.; Yang, C.-S.; Lo, L.-W. Near-Infrared Mesoporous Silica Nanoparticles for Optical Imaging: Characterization and *In Vivo* Biodistribution. *Adv. Funct. Mater.* **2009**, *19*, 215–222.

38. Gorelikov, I.; Matsuura, N. Single-Step Coating of Mesoporous Silica on Cetyltrimethyl Ammonium Bromide-Capped Nanoparticles. *Nano Lett.* **2008**, *8*, 369–373.

39. Saxena, V.; Sadoqi, M.; Shao, J. Degradation Kinetics of Indocyanine Green in Aqueous Solution. *J. Pharm. Sci.* **2003**, *92*, 2090–2097.

40. Topete, A.; Alatorre-Meda, M.; Iglesias, P.; Villar-Alvarez, E. M.; Barbosa, S.; Costoya, J. A.; Taboada, P.; Mosquera, V. Fluorescent Drug-Loaded, Polymeric-Based, Branched Gold Nanoshells for Localized Multimodal Therapy and Imaging of Tumoral Cells. *ACS Nano* **2014**, *8*, 2725–2738.

41. Nasr, C.; Liu, D.; Hotchandani, S.; Kamat, P. V. Dye-Capped Semiconductor Nanoclusters. Excited State and Photosensitization Aspects of Rhodamine 6G H-Aggregates Bound to SiO$_2$ and SnO$_2$ Colloids. *J. Phys. Chem.* **1996**, *100*, 11054–11061.

42. Fan, Z.; Yang, X.; Li, Y.; Li, S.; Niu, S.; Wu, X.; Wei, J.; Nie, G. Deciphering an Underlying Mechanism of Differential Cellular Effects of Nanoparticles: An Example of Bach-1 Dependent Induction of HO-1 Expression by Gold Nanorod. *Biointerphases* **2012**, *7*, 1–8.

43. Kim, B.; Han, G.; Toley, B. J.; Kim, C. K.; Rotello, V. M.; Forbes, N. S. Tuning Payload Delivery in Tumour Cylindroids Using Gold Nanoparticles. *Nat. Nanotechnol.* **2010**, *5*, 465–472.

44. Philip, R.; P, A.; Baumler, W.; Szeimies, R. M.; Abels, C. Absorption and Fluorescence Spectroscopic Investigation of Indocyanine Green. *J. Photochem. Photobiol., A* **1996**, *96*, 137–148.

45. Shen, S.; Tang, H.; Zhang, X.; Ren, J.; Pang, Z.; Wang, D.; Gao, H.; Qian, Y.; Jiang, X.; Yang, W. Targeting Mesoporous Silica-Encapsulated Gold Nanorods for Chemo-Photothermal

Therapy with Near-Infrared Radiation. *Biomaterials* **2013**, *34*, 3150–3158.

46. Sanchez-Valencia, J. R.; Aparicio, F. J.; Espinos, J. P.; Gonzalez-Elipe, A. R.; Barranco, A. Rhodamine 6G and 800 J-Heteroaggregates with Enhanced Acceptor Luminescence (HEAL) Adsorbed in Transparent SiO$_2$ GLAD Thin Films. *Phys. Chem. Chem. Phys.* **2011**, *13*, 7071–7082.

47. Wang, L. V.; Hu, S. Photoacoustic Tomography: *In Vivo* Imaging from Organelles to Organs. *Science* **2012**, *335*, 1458–1462.

48. Jokerst, J. V.; Thangaraj, M.; Kempen, P. J.; Sinclair, R.; Gambhir, S. S. Photoacoustic Imaging of Mesenchymal Stem Cells in Living Mice *via* Silica-Coated Gold Nanorods. *ACS Nano* **2012**, *6*, 5920–5930.

49. Song, C. W.; Park, H. J.; Lee, C. K.; Griffin, R. Implications of Increased Tumor Blood Flow and Oxygenation Caused by Mild Temperature Hyperthermia in Tumor Treatment. *Int. J. Hyperthermia* **2005**, *21*, 761–767.

50. Li, Y.; Zhou, Y.; Wang, H. Y.; Perrett, S.; Zhao, Y.; Tang, Z.; Nie, G. Chirality of Glutathione Surface Coating Affects the Cytotoxicity of Quantum Dots. *Angew. Chem., Int. Ed. Engl.* **2011**, *50*, 5860–5864.

51. Zhao, B.; Yin, J. J.; Bilski, P. J.; Chignell, C. F.; Roberts, J. E.; He, Y. Y. Enhanced Photodynamic Efficacy towards Melanoma Cells by Encapsulation of Pc4 in Silica Nanoparticles. *Toxicol. Appl. Pharmacol.* **2009**, *241*, 163–172.

52. Johnson, P. B.; Christy, R. W. Optical Constants of Noble Metals. *Phys. Rev. B: Solid State* **1972**, *6*, 4370–4379.

53. Razansky, D.; Buehler, A.; Ntziachristos, V. Volumetric Real-Time Multispectral Optoacoustic Tomography of Biomarkers. *Nat. Protoc.* **2011**, *6*, 1121–1129.